



# Communication

## *In Situ* Observation of Martensite Lath Growth Behaviors in the Coarse Grained Heat-Affected Zone of 1.25Cr-0.5Mo Heat-Resistant Steel During Simulated Welding

YANG SHEN and CONG WANG

In the present work, the nucleation and growth of martensite laths in the coarse grained heat-affected zone of 1.25Cr-0.5Mo steel have been systematically studied by high-temperature confocal scanning laser microscope. It is found that martensite laths preferentially nucleate on, in an increasing order of difficulty, grain boundaries, inclusions, and grain interior. However, their growth rates are governed by the degree of supercooling, and vary over a wide range from 9.4 to 162.4  $\mu\text{m/s}$ .

<https://doi.org/10.1007/s11661-019-05420-9>

© The Minerals, Metals & Materials Society and ASM International 2019

---

Ferrite heat-resistant steels, such as 1.25Cr-0.5Mo steel, offer a combination of high-temperature stability, outstanding creep strength, and eminent corrosion resistance, and are extensively employed in petrochemical, petroleum refining and fossil fired power generating industries.<sup>[1–3]</sup> Fusion welding techniques, such as shielded metal arc welding (SMAW), flux-cored arc welding (FCAW), and submerged arc welding (SAW), are invariably necessitated to weld such heat-resistant grade steels.<sup>[4]</sup> However, the microstructures and mechanical properties of the parent 1.25Cr-0.5Mo steel is susceptible to drastic changes during welding thermal cycle. Especially in the coarse grain heat-affected zone (CGHAZ) of the welded joint, which experiences high peak temperature ( $T_p \gg A_{c3}$ ) and rapid cooling rate,<sup>[5–8]</sup> noticeable phase changes, including diffusive austenitic transformation and diffusionless martensitic transformation, may likely occur.<sup>[9]</sup> Martensite, which is

the main microstructure of the CGHAZ, is of practical importance tuning toughness and strength.<sup>[10]</sup> Consequently, an in-depth understanding of the martensite phase transformation in the CGHAZ is indispensable to secure the overall performance of the weldment.

Previous studies elucidated the phase transformations of the CGHAZ from the viewpoints of morphology and crystallography.<sup>[11–13]</sup> Wang *et al.*<sup>[9]</sup> systematically studied the heterogeneous microstructures of the heat-affected zone in as-welded 9Cr-1Mo-V-Nb steel and revealed that the CGHAZ exhibited the highest hardness. Sarizam *et al.*<sup>[14]</sup> investigated the effect of holding temperature on the variant selection mechanism during bainite transformation in 2Cr-1Mo steel. Yue *et al.*<sup>[15]</sup> and Shome *et al.*<sup>[16]</sup> mainly focused on the effects of different cooling rates on the microstructure of CGHAZ during continuous cooling transformation process, without considering the effects of absolute temperature. However, most of the above results were based on *ex situ* observation.

Fortunately, in recent years, confocal scanning laser microscope (CSLM), a powerful *in situ* observation method, has enabled investigations over the kinetic process of phase transformation and microstructure evolution in steels at high-temperature.<sup>[17–19]</sup> Yin *et al.*<sup>[20]</sup> studied the transformation kinetics from  $\delta$ -ferrite to  $\gamma$ -austenite and found that the incoherent  $\delta/\gamma$  interphase boundaries were always unstable with finger-like morphology, which showed a good agreement between experimental observations and theoretical calculations. Yu *et al.*<sup>[21]</sup> investigated the microstructure evolution during CGHAZ thermal cycling of blast-resistant steel and confirmed the concurrent refinement of martensite packet size with smaller austenite grain size. Mao *et al.*<sup>[22]</sup> revealed five nucleation modes and six types of growth behaviors of bainite laths in reheated weld metals. These studies unanimously demonstrated CSLM as a direct yet powerful tool for simulating actual welding processes.

Nevertheless, until now, there seems to be no *in situ* observations and quantifications of the grain nucleation and growth in the CGHAZ of 1.25Cr-0.5Mo steel through CSLM. An understanding of the growth rate of individual martensite lath is necessary in order to optimize welding parameters to avoid the formation of deleterious microstructures such as transgranular martensite, which can potentially improve the performance of the CGHAZ.<sup>[23]</sup> Therefore, the objective of the present work is to characterize the transients in microstructural changes and the kinetics process of nucleation and growth of martensite and crystallographic orientations in the CGHAZ of 1.25Cr-0.5Mo steel in conjunction with *in situ* CSLM observation and *ex situ* electron backscattered diffraction (EBSD) examination.

1.25Cr-0.5Mo steel plate (ASTM A378 Grade 11 Class 2) with 26-mm thickness was used as the target

---

YANG SHEN and CONG WANG are with the School of Metallurgy, Northeastern University, Shenyang, 110819, P.R. China. Contact e-mail: wangc@smm.neu.edu.cn

Manuscript submitted May 21, 2019.

Article published online August 22, 2019

**Table 1. Chemical Composition of 1.25Cr-0.5Mo Steel (Weight Percent)**

C	Si	Mn	Cu	Ni	Cr	Mo	P	S
0.13	0.59	0.54	0.04	0.02	1.12	0.572	0.017	0.003

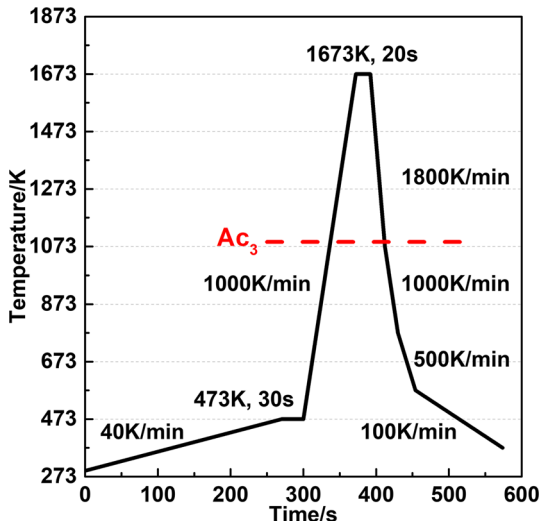


Fig. 1—Thermal cycle for *in situ* observation under CSLM.

material. It was normalized at 1203 K for 52 minutes and tempered at 1033 K for 91 minutes. The chemical composition of the adopted steel is shown in Table I.

The *in situ* observation experiment was conducted by CSLM (VL2000DX-SVF18SP, Yonekura Manufacturing Corporation, Japan). The sample was machined into cylindrical specimen with the dimension of  $\Phi 5 \times 4$  mm. After conventional mechanical grinding and polishing, the specimen was positioned in an alumina crucible, which was placed inside the furnace chamber on a Pt sample holder. The laser light with a wavelength of 405 nm was used to focus and scan at the specimen surface under high purity argon. Successive images were recorded at a rate of 15 frames per second and were collected by a charge-couple device (CCD) camera. The programmed thermal cycle is shown in Figure 1. The specimen was heated to 473 K at a rate of 40 K/min, held for 30 seconds, heated to 1673 K ( $T_p \gg Ac_3 = 1089$  K) at 1000 K/min, and held for 20 seconds. Subsequently, cooling rate was designed as follows: 1673 K to 1073 K, 1800 K/min; 1073 K to 773 K, 1000 K/min; 773 K to 573 K, 500 K/min; 573 K to room temperature, 100 K/min. This thermal cycle was designed especially for simulating the thermal cycle of CGHAZ in SMAW process with 18 kJ/cm heat input.

The specimen after *in situ* observation was prepared by standard metallographic procedures. The crystallographic features were revealed by a field-emission scanning electron microscope (SEM, TESCAN, MAIA3 XMH, CZ) operating at 20.0 kV, which is coupled with an EBSD with the sample stage being tilted by 70 deg and fitted with NordlysMax<sup>3</sup> detector (Oxford Instruments) and HKL CHANNEL5 software. More detailed

description of preparing EBSD specimen is presented elsewhere.<sup>[24]</sup>

Figure 2 shows typical CSLM snapshots of the specimen during cooling from 747 K to 677 K, where most of the expected phase transformations, characterized by distinctive martensite nucleation events, will likely occur. As shown by the red, green, and blue circles in Figures 2(a) through (c), martensite phase transformation occurs according to the apparent surface relief by the displacive motion of austenite to martensite.<sup>[25–27]</sup> It is found that martensite laths preferentially nucleate on, in order of increasing difficulty, grain boundaries, inclusions, and grain interior, as highlighted by red, green, and blue dotted squares in the inset of Figures 2(a) through (c). It is well known that martensitic transformation preferentially nucleates where the energy barrier is lower. Risk *et al.*<sup>[28]</sup> stated that the energy barrier for heterogeneous nucleation on the surface of inclusion was generally higher than that of on the grain boundaries. They also demonstrated the larger inclusions are more energetically favorable than the smaller ones. Moreover, the influence of chemical composition of inclusions on martensite formation is determined, in most cases, by the strain incurred *via* lattice mismatch between inclusions and the matrix. Xu *et al.*<sup>[29]</sup> reported that the energy barrier for homogeneous nucleation on the free surface in the austenite matrix was the highest. In our present study, martensites are revealed, for the first time, to nucleate on the three distinctive nucleation sites in the CGHAZ of 1.25Cr-0.5Mo steel, which are aligned and consistent with the results of previous studies.<sup>[30,31]</sup>

Moreover, growth characteristics of martensite laths at the corresponding nucleation sites have been documented in Figures 2(d) through (h). The first martensite lath ( $M_1$ ) nucleates on the grain boundary and grows in a direction of 20 deg inclined to it. Subsequent martensite laths nucleate at the tip of existing laths, and grow in parallel to the existing lath, as shown by the red dotted squares in the inset of Figures 2(d) through (f). The second martensite lath ( $M_2$ ), as shown by the green circle in Figure 2(d), nucleates at the inclusion inside a grain. With the increase of cooling time, as displayed by the green dotted squares in the inset of Figures 2(d) through (f), it can be clearly seen that some newly formed martensite laths are always attached to the previous lath. On the other hand, some newly formed martensite laths grow in the opposite direction, which is represented by the green arrows in the inset of Figures 2(e) and (h). The third martensite lath ( $M_3$ ), as shown by the blue circle in Figures 2(e) and (f), starts to nucleate inside the grain at 710.3 K and stops by impinging on another martensite lath (white dash line in Figure 2(f)) at 697.8 K. As shown by the blue circles in Figures 2(g) and (h), the fourth martensite lath ( $M_4$ )

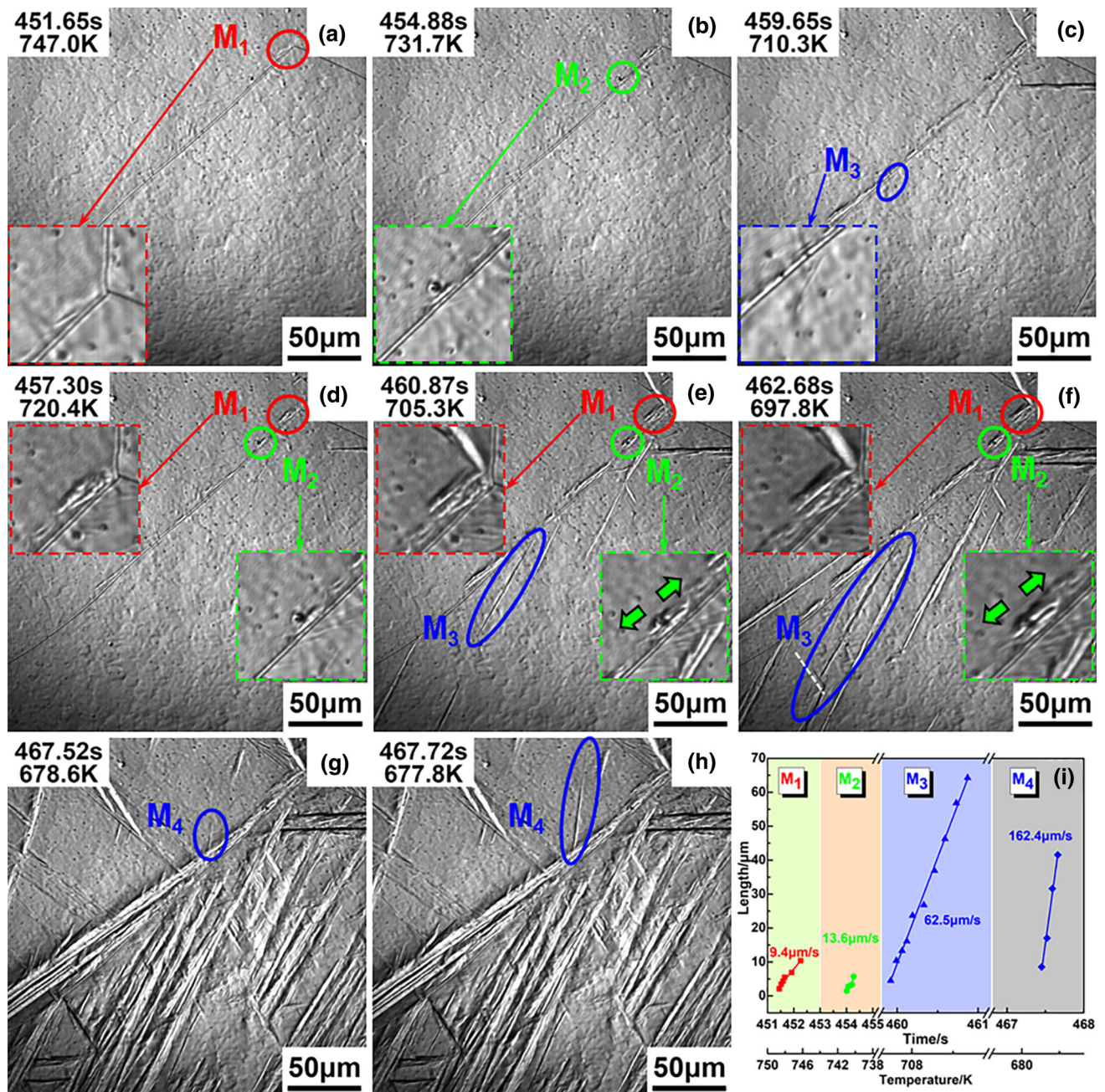


Fig. 2—(a) through (h) CSLM snapshots tracking the continuous growth of martensite laths; (i) the relationship between growing martensite length against cooling time for the four martensite laths. (Red, green, and blue circles show the three nucleation sites, respectively; M<sub>1</sub>, M<sub>2</sub>, M<sub>3</sub>, and M<sub>4</sub> represent the first, second, third, and fourth martensite lath, respectively) (Color figure online).

nucleates inside the grain at 678.6 K and then extends at a high rate in the grain.

The detailed measurement results of growth rates of the four martensite laths are shown in Figure 2(i). The measurement of the length of the martensite lath begins at the moment of its nucleation, which was measured from CSLM images using the Image J software.<sup>[32]</sup> The growth rates of the four martensite laths (M<sub>1</sub>, M<sub>2</sub>, M<sub>3</sub>, and M<sub>4</sub>) are 9.4, 13.6, 62.5, and 162.4 μm/s, respectively. Furthermore, it is observed that the growth rate of martensite lath sharply increases with the decreasing

temperature. It is well known that the energy barriers for different martensite nucleation sites, which only affect the order of martensite nucleation. The difference in growth rate for the four martensite laths is mainly determined by the difference in temperature. Comparing the growth rate of M<sub>3</sub> (62.5 μm/s) and M<sub>4</sub> (162.4 μm/s) in Figure 2(i), it can be confirmed that, although the nucleation sites (grain interior) for both M<sub>3</sub> and M<sub>4</sub> are akin to each other, respective growth rate differs significantly with the temperature (M<sub>3</sub> and M<sub>4</sub> grow at 710.3 K and 678.6 K, respectively).

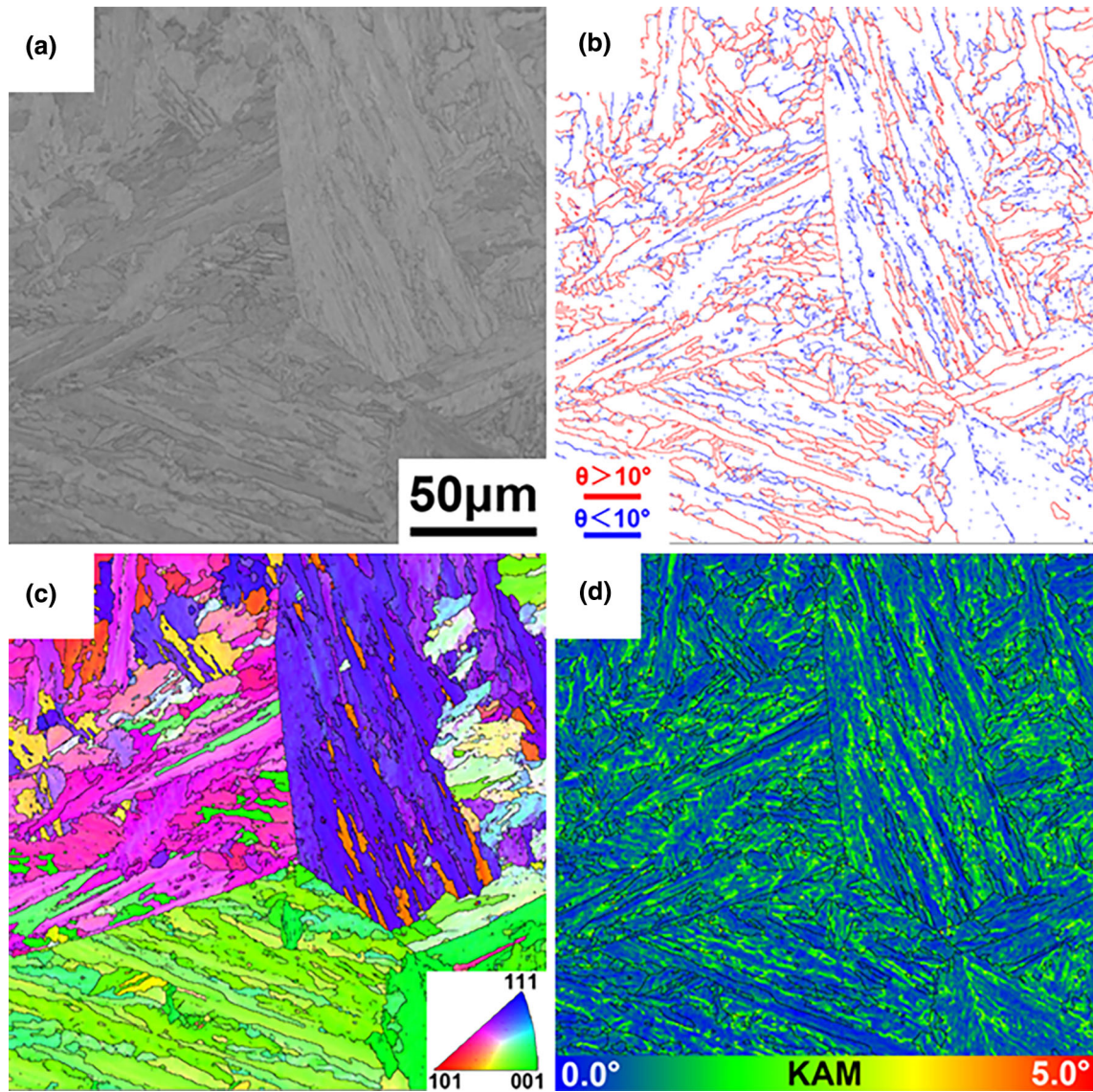


Fig. 3—Crystallographic features of CGHAZ analyzed by EBSD: (a) band contrast map, (b) grain boundary map, (c) invers pole figure, and (d) kernel average misorientation map.

Therefore, four typical growth rates, highlighted by different shadow colors, are summarized in Figure 2(i). The main reason responsible for the great difference in growth rates is probably the difference in the driving force for the martensitic transformation, which is caused by the degree of supercooling. The driving force for martensite transformation differs from the region with many nucleation sites and the region with less nucleation sites. Celada-Casero *et al.*<sup>[33]</sup> reported that the martensite transformation rate increases due to the higher density of nucleation sites and indicated that the formation of larger fractions of martensite requires greater supercooling. It is widely accepted that the extent of martensite transformation as a function of temperature can be well described by the Koistinen and Marburger Eq. [1]<sup>[34–37]</sup>:

$$f = 1 - \exp[-\alpha_m(M_S - T)] \quad [1]$$

where  $f$  is the volume fraction of martensite in the sample at a temperature  $T$  below  $M_S$ , and  $\alpha_m$  is a constant.

According to Eq. [1], with the decrease of temperature, the fraction of martensite will increase. The previous martensite laths provide a large number of nucleation sites for subsequent growth of martensite laths. Thus, the great difference in growth rates could be attributed to the degree of supercooling.

Martensite transformation kinetics has been studied through *in situ* CSLM observations. Detailed *ex situ* crystallographic observations by EBSD are exhibited in Figure 3. Figure 3(a) shows a typical lath martensitic microstructure within the prior austenite grains (PAGs)

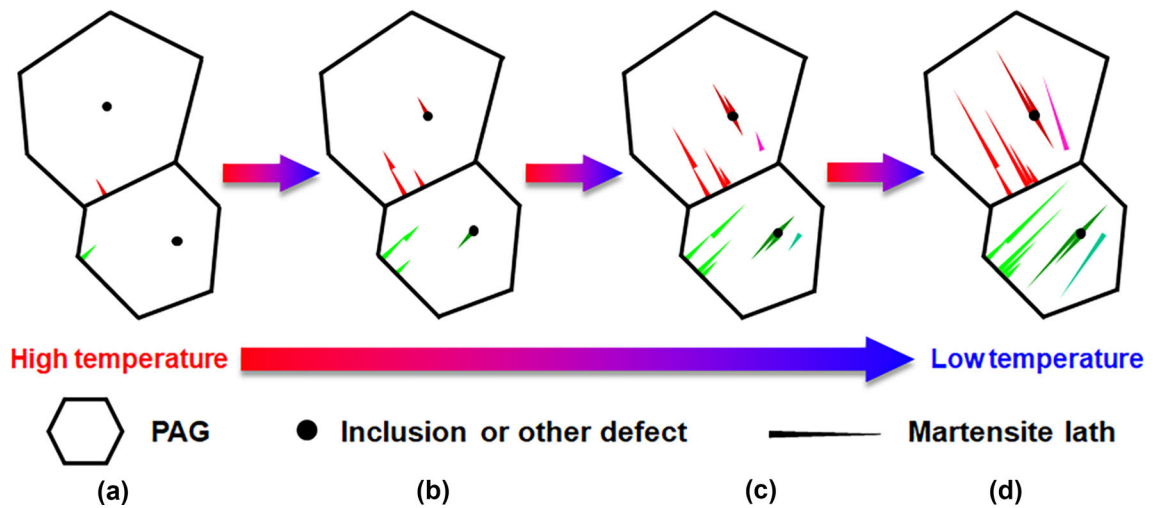


Fig. 4—Schematic illustration of the martensite transformation: (a) nucleate on grain boundary; (b) nucleate on inclusion or other defect; (c) nucleate on grain interior; (d) growth of martensite lath.

after the thermal cycle of a simulated CGHAZ by CSLM. Grain boundary map in Figure 3(b) illustrates the multiple boundary structure, and misorientation boundaries of 2 to 10 deg and over 10 deg are defined as low angle grain boundaries (LAGBs) and high angle grain boundaries (HAGBs), respectively. The PAGBs are mostly HAGBs, and the sub-boundaries within the PAGs are partly LAGBs, such as fine lath martensite boundaries. Normalized frequency of HAGBs is 60.7 pct, while that of low angle grain boundaries (LAGBs) is 39.3 pct. As clearly displayed in the inverse pole figure (Figure 3(c)), the crystal orientation of martensite laths in the same PAG is substantially the same, and the misorientation of martensite laths in different PAGs varies widely. Kernel average misorientation (KAM) map is a measure of local grain misorientation.<sup>[38]</sup> KAM map in Figure 3(d) shows the high local strain levels or crystal deformations of the grains, which indicate the high degree of the martensitic transformation in the CGHAZ.

Quantitative characterization in the CGHAZ of 1.25Cr-0.5Mo steel enables a clearer understanding of how the microstructure evolves during welding. Based on the results above, a schematic illustration of the martensite transformation is illustrated in Figure 4. It can be clearly seen that the order of the martensite nucleation site is evolving from grain boundaries (Figure 4(a)), to inclusions/other defects (Figure 4(b)), and to the interior of the grains (Figure 4(c)). It has also been suggested that the new martensite laths tend to nucleate at the tip or the side of previous martensite, and grow in parallel to the existing lath. Moreover, regardless of the order of nucleation, the crystallographic orientation of martensite laths in the same PAG is substantially the same. During continuous cooling of the welding process, the growth rate of martensite lath

sharply increases with decreasing temperature, as shown in Figures 4(a) through (d), which could be attributed to the degree of supercooling.

In this work, a powerful method, *in situ* CSLM observation, has been utilized to track the microstructure evolution in the CGHAZ of 1.25Cr-0.5Mo steel during the cooling process, and the kinetics process of nucleation and growth of martensite laths has been systematically characterized. Main results are as follows:

- (1) *In situ* observations suggested that three nucleation sites of martensite laths in the CGHAZ are put forward, which are considered to be on grain boundaries, inclusions, and grain interior, respectively.
- (2) With the decreasing temperature, the growth rates of martensite laths vary over a wide range, from 9.4 to 162.4  $\mu\text{m/s}$ , which could be attributed to the degree of supercooling.

---

The authors wish to thank the financial supports from National Natural Science Foundation of China (51622401, 51628402, 51861145312, 51861130361), National Key Research and Development Program of China (2016YFB0300602), The Fundamental Research Fund for Central Universities (N172502004, N182506002), State Key Laboratory of Solidification Processing, Northwestern Polytechnical University (SKLSP201805), and Global Talents Recruitment Program endowed by the Chinese Government. The authors also greatly appreciate the support from Dr. Tongsheng Zhang from Central South University.

## REFERENCES

1. N. Gope, T. Mukherjee, and D.S. Sarma: *Metall. Mater. Trans. A*, 1992, vol. 23A, pp. 221–35.
2. B. Raj, B.K. Choudhary, and R.K.S. Raman: *Int. J. Press. Vessels Pip.*, 2004, vol. 81, pp. 521–34.
3. K. Yagi, G. Merckling, T.U. Kern, H. Irie, and H. Warlimont: *Creep Properties of Heat Resistant Steels and Superalloys*, 2004th ed., Springer, Berlin, Heidelberg, 2004, pp. 62–66.
4. J.A. Francis, W. Mazur, and H.K.D.H. Bhadeshia: *Mater. Sci. Technol.*, 2006, vol. 22, pp. 1387–95.
5. Y. Li and T.N. Baker: *Mater. Sci. Technol.*, 2010, vol. 26, pp. 1029–40.
6. C.L. Davis and J.E. King: *Metall. Mater. Trans. A*, 1994, vol. 25A, pp. 563–573.
7. E. Bonnevie, G. Ferrière, A. Ikhlef, D. Kaplan, and J.M. Orain: *Mater. Sci. Eng. A*, 2004, vol. 385, pp. 352–58.
8. X. Zou, J. Sun, D. Zhao, H. Matsuura, and C. Wang: *J. Iron Steel Res. Int.*, 2018, vol. 25, pp. 164–72.
9. Y. Wang, R. Kannan, and L. Li: *Mater. Charact.*, 2016, vol. 118, pp. 225–34.
10. T. Swarr and G. Krauss: *Metall. Mater. Trans. A*, 1976, vol. 7A, pp. 41–48.
11. Y. Shen, J. Leng, and C. Wang: *J. Mater. Sci. Technol.*, 2019, vol. 35, pp. 1747–52.
12. H. Terasaki and Y.-I. Komizo: *Metall. Mater. Trans. A*, 2013, vol. 44A, pp. 2683–89.
13. C. Zhang, L. Cui, Y. Liu, C. Liu, and H. Li: *J. Mater. Sci. Technol.*, 2018, vol. 34, pp. 756–66.
14. M. Sarizam and Y. Komizo: *J. Mech. Eng. Sci.*, 2013, vol. 7, pp. 1103–14.
15. X. Yue, J.C. Lippold, B.T. Alexandrov, and S.S. Babu: *Weld. J.*, 2012, vol. 91, pp. 67s–75s.
16. M. Shome and O.N. Mohanty: *Metall. Mater. Trans. A*, 2006, vol. 37A, pp. 2159–69.
17. D. Phelan, M. Reid, and R. Dippenaar: *Metall. Mater. Trans. A*, 2006, vol. 37A, pp. 985–94.
18. X. Zou, J. Sun, H. Matsuura, and C. Wang: *Metall. Mater. Trans. B*, 2018, vol. 49B, pp. 2168–73.
19. W. Mu, P. Hedström, H. Shibata, P.G. Jönsson, and K. Nakajima: *JOM*, 2018, vol. 70, pp. 2283–95.
20. H. Yin, T. Emi, and H. Shibata: *Acta Mater.*, 1999, vol. 47, pp. 1523–35.
21. X. Yu, S.S. Babu, J.C. Lippold, H. Terasaki, and Y.I. Komizo: *Metall. Mater. Trans. A*, 2012, vol. 43A, pp. 1538–46.
22. G. Mao, R. Cao, X. Guo, Y. Jiang, and J. Chen: *Metall. Mater. Trans. A*, 2017, vol. 48A, pp. 5783–98.
23. S.M.C. Van Bohemen and J. Sietsma: *Mater. Sci. Eng. A*, 2010, vol. 527, pp. 6672–76.
24. Y. Shen and C. Wang: *Metall. Mater. Trans. B*, 2019, vol. 50B, pp. 595–600.
25. H. Bhadeshia and R. Honeycombe: *Steels: Microstructure and Properties*, 3rd ed., Butterworth-Heinemann, Oxford, 2017, pp. 95–112.
26. G. Miyamoto, N. Takayama, and T. Furuhashi: *Scr. Mater.*, 2009, vol. 60, pp. 1113–16.
27. H. Kitahara, R. Ueji, N. Tsuji, and Y. Minamino: *Acta Mater.*, 2006, vol. 54, pp. 1279–88.
28. R. Ricks, P. Howell, and G. Barritte: *J. Mater. Sci.*, 1982, vol. 17, pp. 732–40.
29. Z. Xu, X. Jin, and J. Zhang: *Phase Transformation in Materials*, 1st ed., Higher Education Press, Beijing, 2013, pp. 87–99.
30. G. Ghosh and G.B. Olson: *Acta Mater.*, 1994, vol. 42, pp. 3361–70.
31. G.B. Olson and M. Cohen: *Metall. Trans. A*, 1976, vol. 7, pp. 1905–14.
32. C.A. Schneider, W.S. Rasband, and K.W. Eliceiri: *Nat. Methods*, 2012, vol. 9, pp. 671–75.
33. C. Celada-Casero, J. Sietsma, and M.J. Santofimia: *Mater. Des.*, 2019, vol. 167, pp. 1–10.
34. S.M.C. Van Bohemen, J. Sietsma, M.J.M. Hermans, and I.M. Richardson: *Acta Mater.*, 2003, vol. 51, pp. 4183–96.
35. S.M.C. Van Bohemen and J. Sietsma: *Metall. Mater. Trans. A*, 2009, vol. 40A, pp. 1059–68.
36. S.M.C. Van Bohemen and J. Sietsma: *Mater. Sci. Technol.*, 2014, vol. 30, pp. 1024–33.
37. X. Zhou, C. Liu, L. Yu, Y. Liu, and H. Li: *J. Mater. Sci. Technol.*, 2015, vol. 31, pp. 235–42.
38. L. Saraf: *Microsc. Microanal.*, 2011, vol. 17, pp. 424–25.

**Publisher's Note** Springer Nature remains neutral with regard to jurisdictional claims in published maps and institutional affiliations.